

# Elucidating intercalation of transition metal guests to tailor properties of layered MXenes

Shianlin Wee<sup>1</sup>, Xiliang Lian<sup>2,3</sup>, Dario Gomez Vazquez<sup>1</sup>, Mathieu Salanne<sup>2,3,4,\*</sup>, Maria R. Lukatskaya<sup>1,\*</sup>

1. Electrochemical Energy Systems Laboratory, Department of Mechanical and Process Engineering, ETH Zurich, 8092 Zurich, Switzerland.

2. Sorbonne Université, CNRS, Physicochimie des Électrolytes et Nanosystèmes Interfaciaux, F-75005 Paris, France.

3. Réseau sur le Stockage Electrochimique de l'Énergie (RS2E), FR CNRS 3459, 80039 Amiens Cedex, France.

4. Institut Universitaire de France (IUF), 75231 Paris, France.

\*Corresponding author email: [mlukatskaya@ethz.ch](mailto:mlukatskaya@ethz.ch)

## ABSTRACT

Transition metal (TM) cations exhibit distinct electronic properties, compared to alkali and alkaline earth metal cations. In this work, we aim to explore the electronic coupling between different redox-active TMs guest and conductive MXene host. Specifically, within the confined environment of MXene layers, different inserted TM cations demonstrate varying electronic structures and exert distinct influences on the MXene. Unlike Cu which undergoes unusual reduction upon insertion within MXenes, our Bader charge analysis and X-ray absorption spectroscopy (XAS) results indicate that the oxidation states of inserted Ni, Co, Mn, and Zn ions remain unchanged. Despite the higher degree of Ti oxidation led to higher resistivity of intercalated MXenes, the density of states analysis of Ni and Co highlighted the important contributions of these TM cation guests on the overall electrical conductivity of intercalated-MXenes. Moreover, the TM-intercalated MXenes displayed varying redox contributions to the charge storage, where the redox properties of transition metal can be suppressed. This study highlights the unique influence of each transition metal cation under MXene confinement and lays the groundwork for utilizing transition metal guests in MXenes for various electrochemical applications.

## INTRODUCTION

MXenes, are an emerging class of 2D transition metal carbides and nitrides with the general formula  $M_{n+1}X_nT_x$ . Here, M represents an early transition metal,  $n = 1-4$ , X is carbon and/or nitrogen, and  $T_x$  refers to surface terminations such as =O, -OH, -Cl, -F.<sup>[1]</sup> By combining tunable metallicity<sup>[1]</sup>, hydrophilicity<sup>[1]</sup>, chemical tunability<sup>[1]</sup> and attractive redox characteristics<sup>[2]</sup>, MXenes show a great promise for diverse applications spanning from energy storage<sup>[2-4]</sup> and electrocatalysis<sup>[5]</sup>, electromagnetic shielding<sup>[6]</sup> to biomedical uses<sup>[7]</sup>. The electronic and electrochemical properties of MXenes are highly tunable through strategic manipulation of their composition<sup>[1]</sup> and structure<sup>[1, 8]</sup>. For example, varying the transition metal (TM) elements within the MX layer and modifying surface terminations significantly impact these properties.<sup>[8]</sup> Furthermore, the layered structure and negatively charged surfaces of MXenes facilitate (electro)chemical intercalation of various cations<sup>[4, 9-10]</sup> and polar molecules<sup>[11]</sup>, offering an additional route to alter their properties.

Despite extensive research on the intercalation of alkali<sup>[4]</sup>, alkaline earth<sup>[4]</sup> and organic cations into MXenes, a very few studies have focused on the intercalation of TM cations. Most of these studies focus on incorporating single atoms or nanoparticles of transition metals (TMs) onto MXene surface<sup>[12-16]</sup>. Therefore, the interfacial interactions and chemistries between TM cations and MXenes within the confined environment between MXene layers remain relatively unexplored. Our prior research shows that intercalation of Cu ions into  $Ti_3C_2T_x$  induced charge distribution within MXene layers, altering their electronic and electrochemical properties.<sup>[17]</sup> Specifically, a unique case of coupled redox and pseudocapacitance for TM guest and MXene host was observed.<sup>[17]</sup>

In this work, we investigated the impact of a wide range of intercalating different redox-active 3d transition metal (TM) cations ( $Mn^{2+}$ ,  $Co^{2+}$ ,  $Ni^{2+}$ ,  $Cu^{2+}$  and  $Zn^{2+}$ ) into  $Ti_3C_2T_x$  MXene host. By systematically varying the

TM identity, we elucidated the influence of electronic configuration on the MXene's electronic and electrochemical properties. A combination of ab initio molecular dynamics (AIMD), density functional theory (DFT), X-ray absorption spectroscopy (XAS), resistivity and electrochemical measurements was employed to comprehensively characterize the resulting physicochemical changes. Finally, using in-situ XAS experiments to monitor the oxidation states changes of TM-intercalated MXenes under varying applied potentials, we reveal that the electrochemical responses of the systems are strongly influenced by the identity of the intercalated TM cations.

## RESULTS AND DISCUSSION

### Electronic structure of a series of TM-intercalated $\text{Ti}_3\text{C}_2\text{T}_x$

First, we performed ab initio molecular dynamics (AIMD) calculations for detailed comparison of how electronic structure of pristine  $\text{Ti}_3\text{C}_2\text{T}_x$  MXene changes upon intercalation of the identical fractions of 0.2  $\text{Ni}^{2+}$ ,  $\text{Co}^{2+}$ ,  $\text{Cu}^{2+}$  and  $\text{Mg}^{2+}$  cations per  $\text{Ti}_3\text{C}_2(\text{OH})_2$  unit.<sup>[17]</sup> The choice of AIMD was motivated by (1) the occurrence of chemical reactions, such as proton transfer, within the materials, that cannot be easily be included in classical MD and (2) the limitations of current force fields in accurately modeling transition metals due to their complex interaction with water and MXenes<sup>[18]</sup>. A systematic approach, detailed in the Methods section, was employed to identify representative configurations. The final compositions of the simulation cells are summarized in **Table S1**.

**Figure 1** depicts typical snapshots of the simulated MXene structures with different intercalated ions. Upon intercalation, the water molecules adopt a bilayer-like structure with increasing interlayer spacing. This reorganization is driven by the hydration of the cations in the interlayer. Notably, we observe distinct spatial arrangements of the cations within the interlayer for each intercalating cation:  $\text{Co}^{2+}$  and  $\text{Mg}^{2+}$  cations reside within the water bilayer, without direct contact with the MXene termination groups, whereas  $\text{Cu}^+$  and  $\text{Ni}^{2+}$  are predominantly coordinated by water oxygen atoms and the MXene surface terminations.

To further understand these structural differences, we calculated the radial distribution functions (RDF) and the coordination numbers (CNs) between cations and oxygen atoms, as shown in **Figure S1**. **Table S2** summarizes the extracted average first neighbor distances and first solvation shell CNs. For all the transition metal cations (TM), the first TM-O distance remains comparable to the bulk solution values, consistent with the prior studies on MXenes intercalated with alkali and alkali-earth metal cations.<sup>[19]</sup> Meanwhile, the CNs of the studied intercalated cations exhibit distinct behaviors compared to bulk solution. Previous studies have shown that alkali and alkali-earth cations experience reduced CNs when confined in interlayer spaces<sup>[19]</sup>. Our findings for  $\text{Mg}^{2+}$  align with these observations, as its CN decreases from 6 in bulk water to 4 in the interlayer environment. For transition metal cations, we see that CNs also decrease upon intercalation. For Cu cations, consistent with our previous findings,<sup>[17]</sup> the CN can drop as low as 2 due to the reduction of  $\text{Cu}^{2+}$  to  $\text{Cu}^+$  upon intercalation. Meanwhile, intercalated  $\text{Ni}^{2+}$  and  $\text{Co}^{2+}$  are coordinated by 3 and 4 oxygen atoms, respectively, compared to CN = 6 in bulk solution<sup>[20-21]</sup>. This suggests that their electronic properties may differ significantly from those of Cu-MXene. Additionally, the coordination shell of  $\text{Co}^{2+}$  is more well-defined compared to  $\text{Ni}^{2+}$ , as indicated by the presence of a plateau for  $\text{Co}^{2+}$  in the CN(r) function (**Figure S1**). This distinction likely arises from their different positions within the interlayer (**Figure 1**).

Next, we calculated the Bader charges for the intercalated TM cations (**Table S3**) and compared them to the those of the corresponding TM oxides. Upon intercalation, Co ions retain a +2 oxidation state, as indicated by its Bader charge of 0.9520, which is close to the value of 1.1650 in CoO. The case of Ni is more complex. The Ni Bader charge in NiO is 1.130, whereas we obtain a value of 0.7191 for the Ni-MXene. Although this might suggest a partial reduction of  $\text{Ni}^{2+}$  upon intercalation, caution is necessary due to the absence of a reliable reference value for  $\text{Ni}^{1+}$ . We propose that the Ni-O bonds formed with the oxygen

atoms of the MXene surface, particularly those bound to oxidized Ti atoms, might induce charge accumulation on the Ni atoms, leading to an artificially low Bader charge. To verify this hypothesis, we performed another calculation where we substituted the Co cations in Co-MXene with Ni cations and then calculated the Bader charges. The resulting Ni average Bader charge is 0.9718, close to that of NiO. This result confirms that the lower Bader charge observed in the initial calculations is likely an artifact of the Bader charge analysis algorithm.

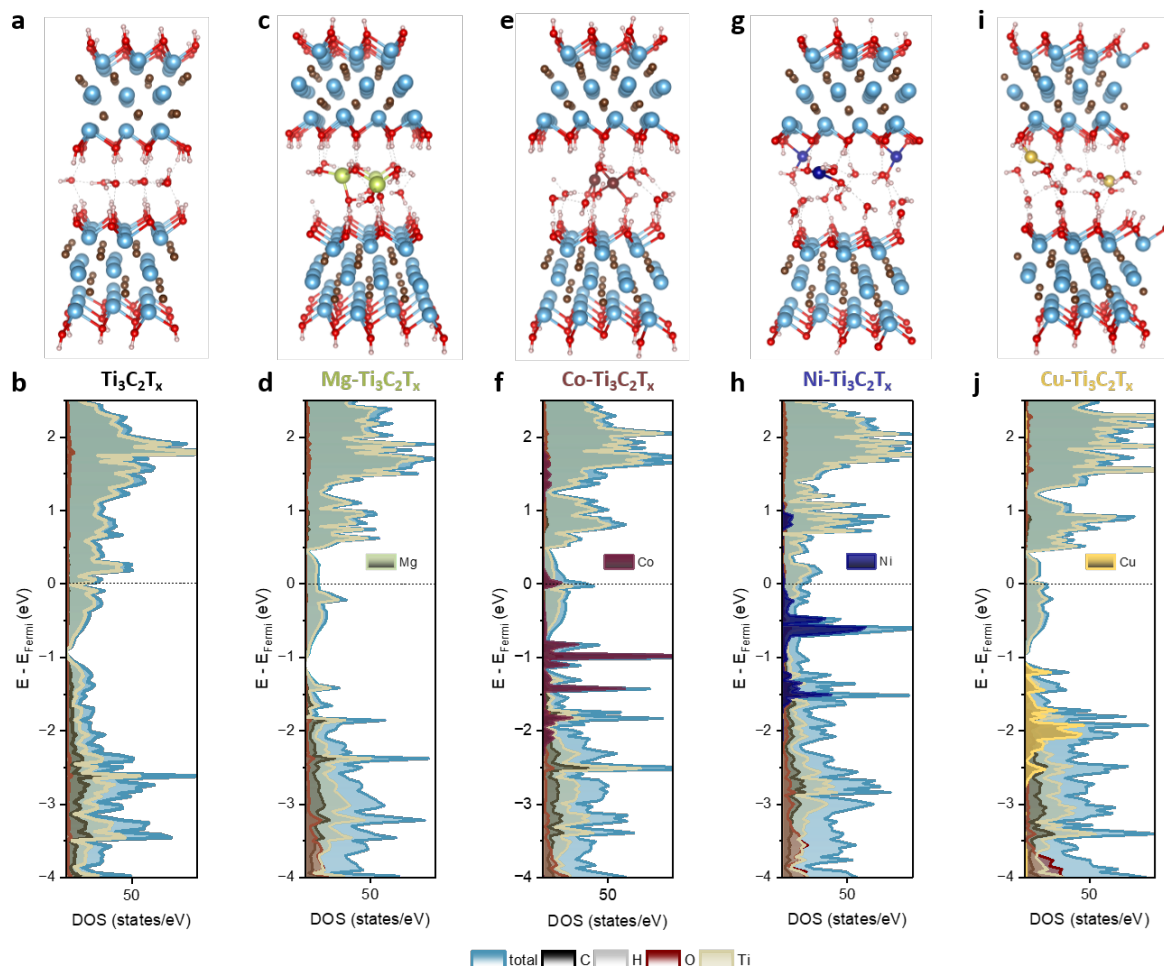


**Figure 1.** Typical snapshots extracted from the simulations of **a.** pristine MXene with a single-layer  $\text{H}_2\text{O}$ , as well as MXenes inserted with 0.2 fraction of intercalated cations including **c.** Mg, **e.** Co, **g.** Ni, and **i.** Cu. The Ti, C, O, and H atoms are displayed in cyan, brown, red and white spheres. The metal cations in between the layer are shown in green, wine, blue, and yellow for Mg, Co, Ni, and Cu, respectively. The corresponding density of states for **b.** pristine MXenes and **d.** Mg, **f.** Co, **h.** Ni, and **j.** Cu-inserted MXenes.

Finally, we analyzed the total density of states (TDOS) and partial density of states (PDOS) of different TM-intercalated MXenes (**Figure 1**). In general, the DOS contributions from Ti, C, and H atoms remain similar to those of pristine MXene. For all cases examined, the DOS at a Fermi level is dominated by Ti contributions, consistent with the metallic nature of the MXenes. As expected, no Mg-related states were observed in the displayed energy range due to its closed-shell electron configuration. In contrast, the 3d orbitals of  $\text{Co}^{2+}$  and  $\text{Ni}^{2+}$  contribute notably to the DOS near and below the Fermi level. However, in case of Cu-MXene, Cu-related DOS contributions are absent at the Fermi level. These important differences underscore the unique ways in which each transition metal influences the DOS of intercalated MXene.

## Characterization of TM-intercalated $\text{Ti}_3\text{C}_2\text{T}_x$

Simulations revealed that different transition metal cations result in distinct electronic structures when intercalated into MXenes. Therefore, to validate our simulation results experimentally, we synthesized Ni-, Co-, Zn-, and Mn-intercalated  $\text{Ti}_3\text{C}_2\text{T}_x$  MXenes. The X-ray diffraction (XRD) patterns (**Figure S2**) revealed a shift of the (002) peak from  $2\theta = 7.9^\circ$  (d-spacing = 11.2 Å) for pristine MXene to approximately  $2\theta = 5.8^\circ$  (d-spacing = 15.2 Å) for TM-intercalated MXenes samples, confirming the successful insertion of TM cations.

To quantify the TMs' content, we employed inductively coupled plasma-optical emission spectrometry (ICP-OES) and scanning electron microscopy (SEM) – energy dispersive X-ray spectroscopy (EDX). The resulting fractions of TMs per unit of  $\text{Ti}_3\text{C}_2\text{T}_x$  were confirmed as follows:  $\text{Ni}_{0.09} \pm 0.003$ ,  $\text{Ni}_{0.13} \pm 0.005$ ,  $\text{Ni}_{0.31} \pm 0.012$ ,  $\text{Co}_{0.09} \pm 0$ ,  $\text{Co}_{0.20} \pm 0.005$ ,  $\text{Zn}_{0.09} \pm 0$ ,  $\text{Mn}_{0.09} \pm 0.008$  (**Figure S3**). The fractions of Zn and Mn cations remained rather low (around 0.09 per unit of  $\text{Ti}_3\text{C}_2\text{T}_x$ ), regardless of the  $\text{Zn}^{2+}$  or  $\text{Mn}^{2+}$  concentration of intercalation solution. These observations highlight that the fraction of intercalated TMs depends not only on the concentration of intercalant's solution and the interactions between transition metal cations and MXenes but also the nature of the TM itself.<sup>[17]</sup> Finally, scanning transmission electron microscope (STEM) – energy dispersive X-ray spectroscopy (EDX) maps show the homogeneous distribution of the TMs within  $\text{Ti}_3\text{C}_2\text{T}_x$  layers and absence of TM nanoparticles on the MXene surface (**Figure S4 - 10**).

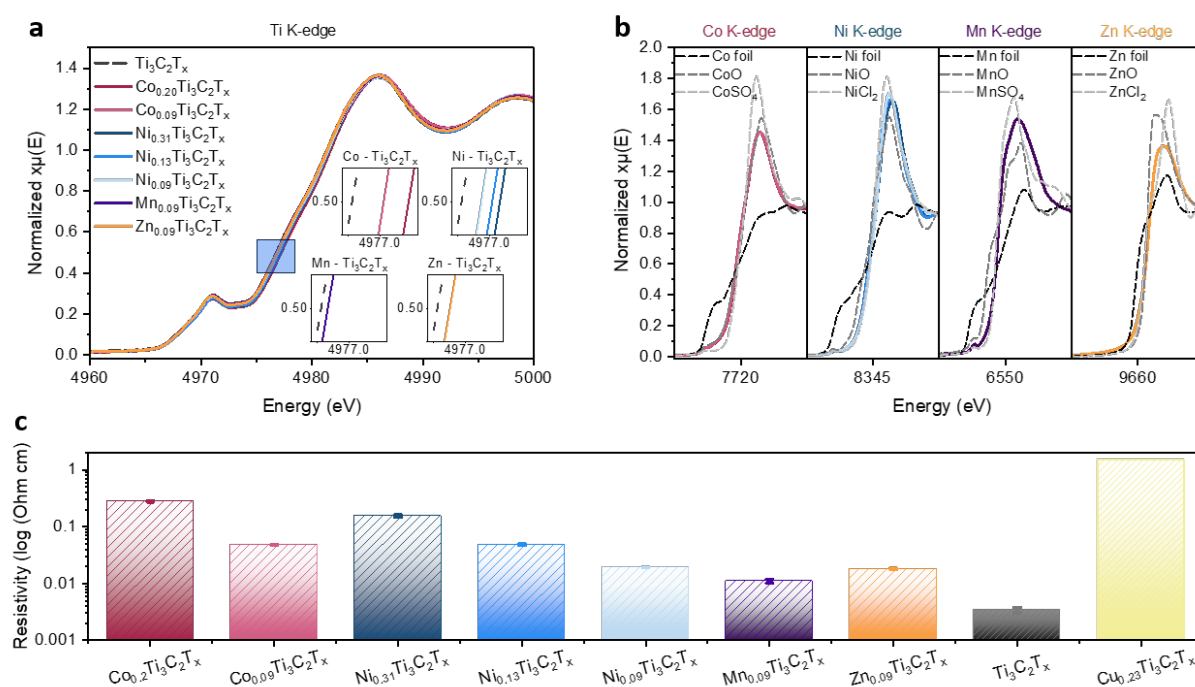


**Figure 2.** a. Normalized X-ray absorption spectra at the Ti K-edge for  $\text{Ti}_3\text{C}_2\text{T}_x$ , Ni- $\text{Ti}_3\text{C}_2\text{T}_x$ , Co- $\text{Ti}_3\text{C}_2\text{T}_x$ , Zn- $\text{Ti}_3\text{C}_2\text{T}_x$ , and Mn- $\text{Ti}_3\text{C}_2\text{T}_x$ . b. Normalized X-ray absorption spectra of Co- $\text{Ti}_3\text{C}_2\text{T}_x$ , Ni- $\text{Ti}_3\text{C}_2\text{T}_x$ , Mn- $\text{Ti}_3\text{C}_2\text{T}_x$  and Zn- $\text{Ti}_3\text{C}_2\text{T}_x$  at their respective inserted transition metal's K-edge. c. Resistivity measurements of pristine and intercalated  $\text{Ti}_3\text{C}_2\text{T}_x$ .

Next, using XAS and conductivity measurements, we investigated the effects of TMs intercalants on the properties of MXenes. For all studied samples, the Ti K-edges shifted to the higher energy compared to the pristine ones, indicating the Ti atoms partially oxidize upon the insertion of guest TM intercalants (Co, Ni, Mn and Zn ions) (**Figure 2a**). This observation aligns with our previous findings, where upon the intercalation of the Cu ions, partial oxidation of Ti atoms takes place.<sup>[17]</sup>

To further explore the relationship between Ti oxidation state and the electrical conductivity of the MXene host, we investigated the influence of (1) different transition metal (TM) intercalants (Co, Ni, Mn, Zn) and

(2) varying the TM intercalant fractions. Our results show that for the same TM, increasing TM intercalant fraction leads to higher Ti oxidation state (**Figure 2a**). The trend is accompanied by a decrease in electrical conductivity, as evidenced by the lower conductivity of  $\text{Ni}_{0.31}\text{Ti}_3\text{C}_2\text{T}_x$ , compared to  $\text{Ni}_{0.13}\text{Ti}_3\text{C}_2\text{T}_x$  and  $\text{Ni}_{0.09}\text{Ti}_3\text{C}_2\text{T}_x$ , and similarly for  $\text{Co}_{0.20}\text{Ti}_3\text{C}_2\text{T}_x$ , compared to  $\text{Co}_{0.09}\text{Ti}_3\text{C}_2\text{T}_x$  samples (**Figure 2c**).

Next, we compared  $\text{Ti}_3\text{C}_2\text{T}_x$  samples intercalated with similar fractions of various TMs (Mn, Zn, Ni, Co). An increase in the Ti K-edge energy, corresponding to higher Ti oxidation state, followed this sequence:  $\text{Mn}_{0.09}\text{Ti}_3\text{C}_2\text{T}_x$ ,  $\text{Zn}_{0.09}\text{Ti}_3\text{C}_2\text{T}_x$ ,  $\text{Ni}_{0.09}\text{Ti}_3\text{C}_2\text{T}_x$ ,  $\text{Co}_{0.09}\text{Ti}_3\text{C}_2\text{T}_x$  (**Figure 2a**). Notably, this trend is mirrored by a corresponding increase in samples resistivity (**Figure 2c**). Finally, we compared conductivity of MXenes with different types of TM and varying fractions to provide an overview of the effects of the TM types and fractions. The following trend in electrical conductivity was observed:  $\text{Ti}_3\text{C}_2\text{T}_x > \text{Mn}_{0.09}\text{Ti}_3\text{C}_2\text{T}_x > \text{Zn}_{0.09}\text{Ti}_3\text{C}_2\text{T}_x > \text{Ni}_{0.09}\text{Ti}_3\text{C}_2\text{T}_x > \text{Co}_{0.09}\text{Ti}_3\text{C}_2\text{T}_x \sim \text{Ni}_{0.13}\text{Ti}_3\text{C}_2\text{T}_x > \text{Ni}_{0.31}\text{Ti}_3\text{C}_2\text{T}_x > \text{Co}_{0.20}\text{Ti}_3\text{C}_2\text{T}_x$ . Simultaneously, the oxidation states of Ti increase in the same sequence (**Figure 2c**). These results suggest that increased oxidation state of Ti MXene can lead to a decrease in charge carrier density near Fermi level, and consequently, results in increased resistivity in TMs-intercalated  $\text{Ti}_3\text{C}_2\text{T}_x$ .<sup>[17]</sup> Nonetheless, it can be seen that the  $\text{Cu}_{0.23}\text{Ti}_3\text{C}_2\text{T}_x$  displayed higher resistivity compared to all other TMs-intercalated MXene, despite its Ti K-edge has lesser shift compared to one of  $\text{Co}_{0.20}\text{Ti}_3\text{C}_2\text{T}_x$  (**Figure S11**). This can be attributed to the different natures and resulting DOS for  $\text{Cu}^{2+}$  when comparing with  $\text{Co}^{2+}$  and  $\text{Ni}^{2+}$ .

Next, we performed XAS at respective TM K-edge to probe the chemical state of intercalated TM cations. XAS revealed that Ni, Co, Mn and Zn cations maintain a +2 oxidation state upon intercalation (**Figure 2b**). This is in contrast to the case of Cu cation intercalation into MXene, which results in charge redistribution and partial reduction of  $\text{Cu}^{2+}$  to approximately +1.3. This difference can be potentially attributed to the electronic configuration of  $\text{Cu}^{2+}$  ion ( $[\text{Ar}]3d^94s^0$ ), that is lacking  $1e^-$  electron to complete its 3d shell. As  $3d^{10}$  configuration is more energetically favorable, upon insertion into highly conductive  $\text{Ti}_3\text{C}_2\text{T}_x$  MXene host, the electron density shifts towards Cu ion guests. This is not the case for other studied TM cations such as  $\text{Ni}^{2+}$  ( $[\text{Ar}]3d^84s^0$ ),  $\text{Co}^{2+}$  ( $[\text{Ar}]3d^74s^0$ ),  $\text{Mn}^{2+}$  ( $[\text{Ar}]3d^54s^0$ ) and  $\text{Zn}^{2+}$  ( $[\text{Ar}]3d^{10}4s^0$ ), as a result, they maintain a valency of + 2.

### Charge storage mechanism of TM-intercalated $\text{Ti}_3\text{C}_2\text{T}_x$

We can therefore expect distinct electrochemical response for each TM-intercalated MXene. Given their higher Co and Ni content,  $\text{Co}_{0.20}\text{Ti}_3\text{C}_2\text{T}_x$  and  $\text{Ni}_{0.31}\text{Ti}_3\text{C}_2\text{T}_x$  MXenes, were selected for further in-depth electrochemical studies using *in situ* XAS to accurately track changes in Co and Ni XAS and quantify their contributions to charge storage. Interestingly, cyclic voltammetry (CV) profiles of  $\text{Co}_{0.20}\text{Ti}_3\text{C}_2\text{T}_x$  show no discernible redox peaks (scan rate of  $1 \text{ mVs}^{-1}$  in 0.1 M NaOH, **Figure 3a, S12**). This contrasts with the case of Cu-intercalated  $\text{Ti}_3\text{C}_2\text{T}_x$ , for which the distinct redox peaks were observed in CVs,<sup>[17]</sup> while *in situ* XAS confirmed the redox activity of Cu ions and their contribution to overall pseudocapacitance of Cu- $\text{Ti}_3\text{C}_2\text{T}_x$  alongside the Ti of MXene host.<sup>[17]</sup>

Next, to elucidate the role of Co ions in the charge storage mechanism of  $\text{Co}_{0.20}\text{Ti}_3\text{C}_2\text{T}_x$ , *in-situ* XAS was employed to investigate the redox changes in both intercalated Co ions and Ti atoms of MXene structure. The linear decrease in Co K-edge energy during cathodic scan, followed by its recovery to the initial position during anodic scan (**Figure 3b, c, S13**), indicates reversible redox reactions of intercalated Co cations. These findings strongly suggest the participation of Co ions in the pseudocapacitive charge storage.

To quantitatively estimate the contributions of Co redox to overall Co- $\text{Ti}_3\text{C}_2\text{T}_x$  capacitance, we correlated Co edge energy shifts to its valency. We can infer that each Co ion gains approximately  $0.2 e^-$  during charging within the voltage window of 0.6 V. The Ti K-edge energy, as expected, showed similar trend (**Figure 3d, e, S14**), revealing an average gain of  $0.08 e^-$  per each  $\text{Ti}_3\text{C}_2\text{T}_x$  due to partial reduction of Ti within the MXene structure during charging. Considering the contributions of both Co and Ti redox, the total electron gain for

each  $\text{Co}_{0.20}\text{Ti}_3\text{C}_2\text{T}_x$  unit is  $0.12 e^-$ , which can be correlated to the redox capacitance of  $90 \text{ F g}^{-1}$ . This value is in excellent agreement with the overall capacitance of  $93 \text{ F g}^{-1}$  calculated from the electrochemistry measurements, confirming the combined contribution of intercalated Co ions and Ti MXene host redox to the charge storage. Importantly, despite distinct differences in their CV profiles, both  $\text{Co-Ti}_3\text{C}_2\text{T}_x$  (this study) and  $\text{Cu-Ti}_3\text{C}_2\text{T}_x$ <sup>[17]</sup> exhibit unique guest-host pseudocapacitance. Moreover, the  $\text{Co}_{0.20}\text{Ti}_3\text{C}_2\text{T}_x$  material demonstrated excellent cycling stability, maintaining 99.5% of its capacitance after 10,000 cycles in 0.1 M NaOH electrolyte (**Figure S15 - 17**).

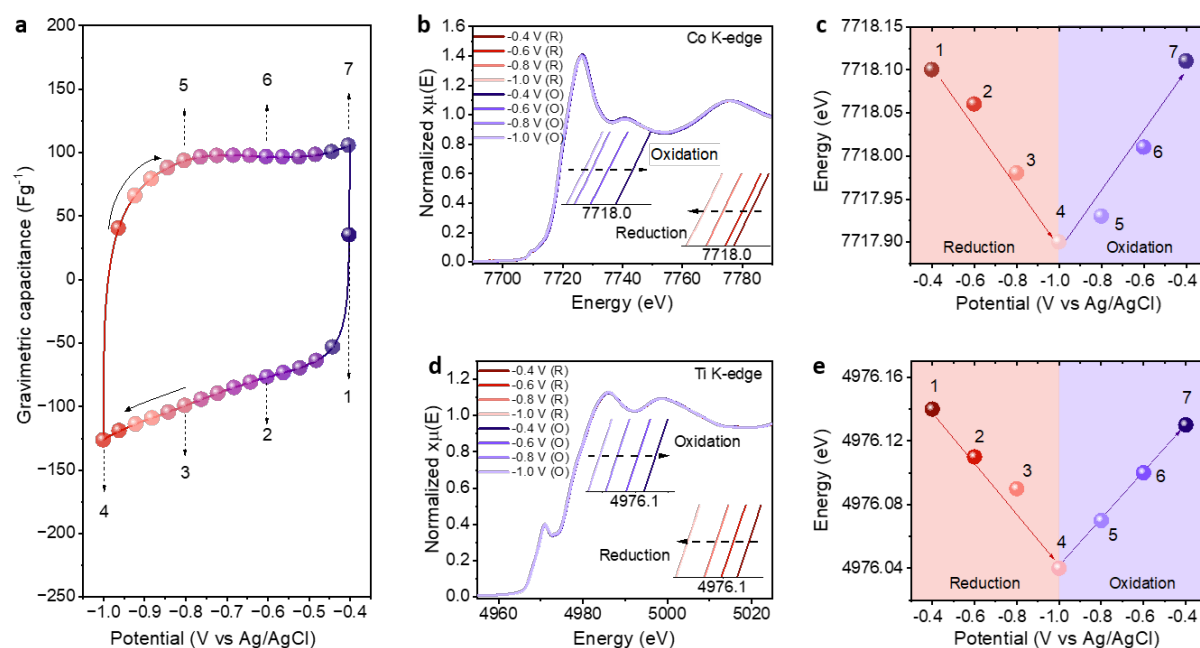


**Figure 3.** (a) CV of  $\text{Co}_{0.20}\text{Ti}_3\text{C}_2\text{T}_x$  at  $1 \text{ mVs}^{-1}$ . In-situ XAS data of  $\text{Co}_{0.20}\text{Ti}_3\text{C}_2\text{T}_x$ : (b) Co K-edge XANES spectra collected at different applied potentials and (c) the variation of Co edge energy with applied potential. (d) Ti K-edge XANES spectra at various reduction and oxidation potentials and (e) the changes in Ti edge energy vs potential during negative and positive potential sweeps.

Given the difference in CV profiles between  $\text{Cu-Ti}_3\text{C}_2\text{T}_x$  (distinct redox CV peak) and  $\text{Co-Ti}_3\text{C}_2\text{T}_x$  (square-shaped CV), fundamental questions arise: Does the absence of redox peaks associated with oxidation state changes in  $\text{Co}_{0.20}\text{Ti}_3\text{C}_2\text{T}_x$  represent a special case? Can general trends be identified for different TM- $\text{Ti}_3\text{C}_2\text{T}_x$  samples? To elucidate this, we used in-situ XAS to study the charge storage mechanism of  $\text{Ni}_{0.31}\text{Ti}_3\text{C}_2\text{T}_x$  as its CV profiles have no pronounced redox peaks, similar to  $\text{Co}_{0.20}\text{Ti}_3\text{C}_2\text{T}_x$  (**Figure 4a, S18**). Interestingly, no notable changes on the Ni K-edge energy were observed for  $\text{Ni}_{0.31}\text{Ti}_3\text{C}_2\text{T}_x$  samples during charge/discharge (**Figure 4b, c**). Meanwhile, the Ti K-edge energy decreased linearly during charging (**Figure 4d, e, S19**), and therefore we can quantify that each  $\text{Ti}_3\text{C}_2\text{T}_x$  gains  $0.18 e^-$  during charging, which can be calculated as redox capacitance value of  $98 \text{ F g}^{-1}$ . This value is very close to  $102 \text{ F g}^{-1}$  that we obtain from electrochemical measurements. These observations suggest that intercalated Ni ions do not exhibit redox and do not contribute to pseudocapacitance after being introduced between MXene layers, and only Ti of  $\text{Ti}_3\text{C}_2\text{T}_x$  actively participates in the charge storage of  $\text{Ni}_{0.31}\text{Ti}_3\text{C}_2\text{T}_x$ . Similar to the  $\text{Co}_{0.20}\text{Ti}_3\text{C}_2\text{T}_x$ ,  $\text{Ni}_{0.31}\text{Ti}_3\text{C}_2\text{T}_x$  demonstrated excellent cycling stability, maintaining 99% of its capacitance and TM loading after 10,000 cycles in 0.1 M NaOH electrolyte (**Figure S20 - 22**).

This observation underscores an intriguing phenomenon: transition metals (TMs) typically considered redox-active may not exhibit expected redox behavior when interacting with a MXene host. These three scenarios presented in this and our previous work reveal key implications: (1) Due to their unique properties, different TMs interact with the MXene host in distinct ways, influencing their contributions to charge

storage. (2) Regardless of the intercalated TM, the redox of Ti-based MXene host consistently dominates overall capacitance.

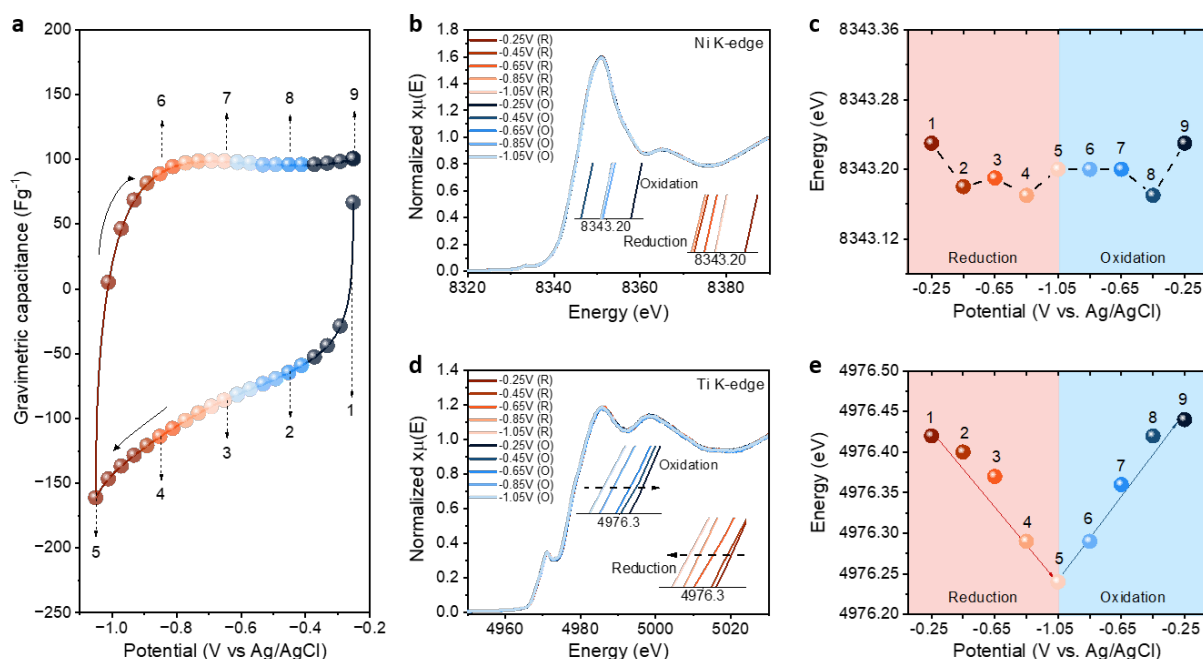


**Figure 4.** a. CV of  $\text{Ni}_{0.31}\text{Ti}_3\text{C}_2\text{T}_x$  at  $1 \text{ mVs}^{-1}$ . Electrochemical XAS data of  $\text{Ni}_{0.31}\text{Ti}_3\text{C}_2\text{T}_x$  where b. Ni K-edge XANES spectra collected during negative and positive potential scans and c. the changes of Ni edge energy with applied potentials. d. Ti K-edge XANES spectra during charging and discharging and e. the variation of Ti edge energy at different applied potentials.

## CONCLUSIONS

In summary, our findings reveal that the intercalation of redox-active transition metal cations into  $\text{Ti}_3\text{C}_2\text{T}_x$  MXene leads to distinct electronic and electrochemical properties. The choice of transition metal significantly influences the MXene's electrical conductivity, as reflected in varying degrees of Ti oxidation and differences in the density of states near the Fermi level under MXene layer confinement. While Cu cations uniquely undergo partial reduction within MXene layers, Ni, Co, Mn, and Zn cations remain in their +2 oxidation state. Moreover, although TMs like Co and Cu can exhibit direct redox contributions to pseudocapacitive charge storage, others such as Ni surprisingly do not. Instead, the redox of Ti in  $\text{Ti}_3\text{C}_2\text{T}_x$  consistently dominates charge storage in these TM-intercalated systems. Overall, our results highlight the potential to fine-tune MXene properties for applications by carefully selecting and controlling TM intercalants. This understanding paves the way for tailoring the properties of  $\text{Ti}_3\text{C}_2\text{T}_x$  MXenes by strategic selection of transition metal cations, enabling their optimization for diverse electrochemical applications and beyond.

## MATERIALS AND METHODS

**Synthesis of  $Ti_3C_2T_x$ .** Both TM-intercalated  $Ti_3C_2T_x$  and  $Ti_3C_2T_x$  MXene were produced following established steps.<sup>[17, 22-23]</sup> To begin, 3 g of  $Ti_3AlC_2$  powder (Carbon-Ukraine, particle size <44  $\mu m$ ) was slowly introduced into a 30 ml etchant solution containing 10 wt% hydrofluoric acid (HF, Sigma-Aldrich, 48 wt%) and approximately 3.3 g of LiCl, maintaining a molar ratio of 5:1 relative to  $Ti_3AlC_2$ . During this process, the Al layers were etched, and  $Li^+$  ions were intercalated into the MXene layers. The solution was then mixed continuously at 350 rpm for 24 hours at 25°C. Following this, the resulting wet sediment was roughly split into 6 portions, each containing 0.5 g of MXene. Each portion underwent 3 rounds of washing with 40 ml of 6 M hydrochloric acid (HCl, Sigma-Aldrich, 37%), with centrifugation at 3500 rpm for 5 min, discarding the supernatant after each wash. Then, the wet sediment was subjected to multiple washes with MiliQ water until a pH of at least 5 was achieved. The non-intercalated  $Ti_3C_2T_x$  powder, referred to as pristine MXene, was collected after these washes, dried via vacuum-assisted filtration, and used for subsequent characterization.

**Preparation of TM-intercalated  $Ti_3C_2T_x$ .** Transition metal cation intercalation into  $Ti_3C_2T_x$  was carried out by mixing 0.5 g of wet  $Ti_3C_2T_x$  sediment with 40 ml of 0.1 M, 0.5 M, 1 M nickel (II) chloride hexahydrate ( $NiCl_2 \cdot 6H_2O$ , Sigma-Aldrich,  $\geq 98\%$ ); 0.5 M, 1 M cobalt (II) chloride hexahydrate ( $CoCl_2 \cdot 6H_2O$ , Sigma-Aldrich, 98%); 0.1 M zinc (II) chloride ( $ZnCl_2$ , Sigma-Aldrich,  $\geq 98\%$ ); 0.1 M manganese (II) chloride tetrahydrate ( $MnCl_2 \cdot 4H_2O$ , Sigma-Aldrich,  $\geq 98\%$ ). After shaking the mixtures for 5 min and settling for 1 hour, the supernatant was discarded via centrifugation at 3500 rpm for 5 mins. Fresh intercalation solution were introduced, and the mixtures were stirred at 300 rpm under an Ar atmosphere for 24 hours at room temperature. The intercalated- $Ti_3C_2T_x$  wet sediments were rinsed thoroughly with MiliQ water three times, and vacuum-dried for 24 hours.

**Electrode preparation.** The preparation of working electrode (WE) and counter electrode (CE) followed the methods outlined in references<sup>[4, 24]</sup>. WE was made of 90 wt.% of MXene powder, 5 wt.% of polytetrafluoroethylene binder (PTFE, Sigma-Aldrich) and 5 wt.% of carbon black (CB, Orion). These components were mixed with excess ethanol using an agate mortar and pestle to form a uniform slurry. Once the ethanol evaporated, the resulting dried slurry was transferred to a clean glass surface. By adding few drops of ethanol, the material was pressed and rolled mechanically into a free-standing film. The CE, comprising 95 wt.% of activated carbon (MTI) and 5 wt.% of polytetrafluoroethylene binder (PTFE, Sigma-Aldrich), was prepared using the similar procedure.

**X-ray diffraction** measurements were conducted using Cu  $K_\alpha$  radiation ( $\lambda = 1.5418\text{\AA}$ , 40 mA and 40 kV) on a PANalytical Empyrean X-ray Powder Diffractometer. Si powder was mixed with all samples except the pristine  $Ti_3C_2T_x$ . The powders were scanned in reflection mode over a  $2\theta$  range from  $4.5^\circ$  to  $60^\circ$ , with a duration of 500 s per each  $0.067^\circ$  acquisition step.

**Scanning transmission electron microscopy (STEM) imaging coupled with energy-dispersive X-ray spectroscopy (EDX) mapping** was acquired using an FEI Talos F200X microscope equipped with an FEI SuperX detector (Chem S/TEM, ScopeM, ETH Zurich), at 200 kV for 5 mins. Prior to acquisition, the powders were ground and dusted onto nickel or copper mesh lacey carbon support films (EMresolutions, Quantifoil).

**Scanning electron microscopy (SEM) images and EDX analyses** were acquired at 20 kV for 5 mins, utilizing Hitachi S-4800 microscope. The MXene powder was spread onto the carbon tape, with excess powder removed using compressed air.

**Inductively coupled plasma optical emission spectrometry (ICP-OES) measurements** were carried out using an Agilent 720 ES instrument. Approximately 5 – 8 mg of TM intercalated- $Ti_3C_2T_x$  powders was dissolved in 5 ml of 20 wt.%  $HNO_3$  (Sigma-Aldrich, 70%) and stirred at 100 rpm for a minimum of 24 hours. After the complete dissolution of MXene powder, the solution was then diluted to 10 wt.%  $HNO_3$  for analysis. Instrument calibrations were conducted before each measurement using solutions of  $CoSO_4$  (Sigma-Aldrich,  $\geq 99\%$ ),  $NiSO_4$  (Sigma-Aldrich,  $\geq 98\%$ ),  $CuSO_4$  (Carl Roth, 99%),  $ZnSO_4$  (Sigma-Aldrich, 99%),  $MnCl_2$  (Sigma-Aldrich,  $\geq 97\%$ ) prepared in 10 wt.% of  $HNO_3$  at TM ion concentrations of 0, 10, 50, and 100 ppm, respectively.

**Resistivity measurements** were performed with an Ossila four-point probe instrument. About 25 mg of MXene powders were pressed using a hydraulic pellet press at 15 MPa, yielding 6-mm-diameter and approximately 0.25-mm-thick pellets.

**Electrochemical set-up and measurements.** Cyclic voltammetry (CV) was carried out in a three-electrode Swagelok cell configuration, using Biologic MPG-200. The WE (free-standing MXene electrode) was placed on a glassy carbon current collector (CH instruments), while the CE (free-standing activated carbon) was placed on a Ti rod current collector. The reference electrode employed was Ag/AgCl in 1M KCl (CH instruments) with 0.1 M NaOH (Sigma-Aldrich, ≥98%) as the electrolyte and a polypropylene membrane (Celgard 3501) as the separator.

**Ex-situ X-ray absorption spectroscopy (XAS)** measurements were carried out at P64 Advanced X-ray Absorption Spectroscopy beamline located at Deutsches Elektronen (DESY) Synchrotron (Hamburg, Germany). The sample preparation steps were as follows: approximately 4 mg of powder sample was mixed homogeneously with about 70 mg of cellulose (Sigma-Aldrich) in an agate mortar. The well-mixed powder was pressed at a 5-ton-force by a pelletizer die set, forming a pellet with thickness of 1 mm and a diameter of 13 mm. Using a Si (111) monochromator, the pellets were assessed in transmission mode for the Ti K-edge; in fluorescence mode with a passivated implanted planar silicon (PIPS) detector for the TM K-edges. Before measuring the pellets, energy calibration was carried out using standard metal foils corresponding to Co (edge at 7.70 keV), Ni (edge at 8.33 keV), Cu (edge at 8.97 keV), Mn (edge at 6.53 keV), Zn (edge at 9.65 keV), and Ti (edge at 4.96 keV). Subsequently, signals for each pellet were obtained through 5 acquisitions at the respective K-edges, with each acquisition lasting approximately 2 min.

**In-situ X-ray Absorption Spectroscopy (XAS)** measurements for Co-Ti<sub>3</sub>C<sub>2</sub>T<sub>x</sub> was carried out at the P64 Advanced X-ray Absorption Spectroscopy beamline at DESY Synchrotron (Hamburg, Germany), while the measurements for Ni-Ti<sub>3</sub>C<sub>2</sub>T<sub>x</sub> were conducted at B18 X-ray Absorption Spectroscopy beamline at Diamond Light Source Synchrotron (Didcot, UK). The Ti and Co K-edges signals for Co-Ti<sub>3</sub>C<sub>2</sub>T<sub>x</sub> were collected in fluorescence mode employing a Si (111) monochromator and a PIPS detector. For Ni-Ti<sub>3</sub>C<sub>2</sub>T<sub>x</sub> sample, the Ti signals were recorded using 4-element Si drift fluorescence detector, while during the collection of Ni signals, 36-element Ge fluorescence detector was used. During data acquisition, the detectors were positioned at 45° angle relative to the MXene electrode within a three-electrode-configuration ECC-Opto-Std test cell (EL-cell, Germany). The in-situ cell incorporated a 50-um-thick polyetherimide sheet coated with 50 nm Au, which served as the current collector and X-ray window for the WE. Similar to previously described electrode preparation steps, the WE consisted of 90 wt.% of Co-Ti<sub>3</sub>C<sub>2</sub>T<sub>x</sub> or Ni-Ti<sub>3</sub>C<sub>2</sub>T<sub>x</sub> powder, 5 wt.% of PTFE, and 5 wt.% of CB. The CE was an over-capacitive activated carbon, the reference electrode was an eDAQ leakless Ag/AgCl (with a filling electrolyte 3.4 M KCl), and the separator was a Celgard 3501 polypropylene membrane. The in-situ cell was cycled for 3 CV cycles at 1 mVs<sup>-1</sup> within the specific potential range of interest (-0.4 V to -1.0 V for Co-Ti<sub>3</sub>C<sub>2</sub>T<sub>x</sub>; -0.25 V to -1.05 V for Ni-Ti<sub>3</sub>C<sub>2</sub>T<sub>x</sub>) before XAS data acquisition. Then, a linear sweep voltammetry (LSV) and approximately 15 min of chronoamperometry (CA) were executed for each relevant potential. A minimum of 3 spectra were acquired at each potential hold, with each acquisition lasting 3 min.

Next, Athena software was used to carry out XAS data analysis. The TM and Ti K-edge energies were determined as the energy at the half-height of the normalized intensity of spectrum<sup>[2, 25-26]</sup>, aligning with the zero of the 2<sup>nd</sup> derivative.<sup>[26-28]</sup> The Ti oxidation states in Co/Ni-Ti<sub>3</sub>C<sub>2</sub>T<sub>x</sub> samples were inferred by correlating Ti edge energy with the Ti valence of TiO (Alfa Aesar, 99.5%) and TiO<sub>2</sub> rutile (Sigma-Aldrich, 99.5%) reference compounds. Similarly, the evaluation of Co or Ni oxidation state involved referencing CoO (Sigma-Aldrich, 99.99%) and Co foil or NiO (Sigma-Aldrich, ≥99.99%) and Ni foil.

Oxidation states changes observed from Co and Ti (in Co-Ti<sub>3</sub>C<sub>2</sub>T<sub>x</sub>), as well as Ti (in Ni-Ti<sub>3</sub>C<sub>2</sub>T<sub>x</sub>) were corroborated with capacitance values derived from CV measurements. The reaction involved can be expressed as:



The capacitance contributions from Ti and TM were calculated using the following formula:  $C_g = \frac{zF}{M_wV}$ , where  $C_g$  is the gravimetric capacitance in F g<sup>-1</sup>,  $z$  is the number of electrons involved,  $F$  is the Faraday's

constant ( $96485 \text{ C mol}^{-1}$ ),  $M_w$  relates to the molar weight in  $\text{g mol}^{-1}$  and  $V$  refers to the potential window in  $V$ .

In the case of  $\text{Co}_{0.20}\text{Ti}_3\text{C}_2\text{T}_x$ , the contributions from Co redox involved  $0.22 \times 0.2 = 0.044$  electrons and for Ti, the value was  $0.026 \times 3 = 0.78$  electrons. The estimated capacitance of  $90 \text{ F g}^{-1}$  (with  $M_w = 213.8 \text{ g mol}^{-1}$ ) closely matches the value of  $93 \text{ F g}^{-1}$  derived from CV data. This confirms that the charge storage mechanism of  $\text{Co}_{0.20}\text{Ti}_3\text{C}_2\text{T}_x$  involves contributions from both Co and Ti redox processes. For  $\text{Ni}_{0.31}\text{Ti}_3\text{C}_2\text{T}_x$ , the electrons participating in Ti redox were estimated to be  $0.06 \times 3 = 0.18$ . The calculated capacitance of  $98 \text{ F g}^{-1}$  (with  $M_w = 220.8 \text{ g mol}^{-1}$ ) aligns well with the CV capacitance of  $102 \text{ F g}^{-1}$ , indicating the charge contribution correlates only to Ti redox.

### **Density Functional Theory (DFT) Calculation and Molecular Dynamics (MD) Simulations**

Although we have different cations and the calculation setup can vary slightly, all calculations generally involve the following three steps: (1) creating the structural model; (2) structural optimization; and (3) ab initio molecular dynamics (AIMD) simulation and properties analysis. In the following paragraphs, we provide a comprehensive explanation of the above steps.

#### **Initial structure generation**

As detailed in our previous work<sup>[17]</sup>, we first reduced the cell size for an affordable computational cost. The reduced cell has 3 formula units of  $\text{Ti}_3\text{C}_2(\text{OH})_2$  and  $\text{H}_2\text{O}$  molecules have been removed. The initial  $c$  lattice parameter is  $12.83 \text{ \AA}$ . In our previous Cu-inserted MXene, we determined the concentration of  $\text{Cu}^{2+}$  is 0.23 per formula unit, which corresponds to 2  $\text{Cu}^{2+}$  ions inserted. Therefore, for all other cations, we fixed the same number of cations to 2. The initial water layer was built using Packmol.<sup>[29]</sup> We treated the two cations as  $\text{Na}^+$  ions and solvated the  $\text{Na}^+$  ions in  $\text{H}_2\text{O}$ . Then, we equilibrated the box using a classical force field in LAMMPS.<sup>[30]</sup> Subsequently, the equilibrated water layer was inserted into the MXene layer and  $\text{Na}^+$  ions were substituted with corresponding cations. Four protons were randomly removed to implicitly assign a +2 charge to the cations. Then, we performed structural relaxation on the models.

#### **Structural optimization**

All our electronic structure calculations were performed within the density functional theory framework as implemented in the Vienna ab initio simulation package (VASP).<sup>[31-32]</sup> The wave functions are expanded in plane wave basis sets and the projector augmented wave (PAW) method is used to describe the core-valence interactions. The exchange-correlation energy is approximated with the generalized gradient approximation as formulated by Perdew, Burke, and Ernzerhof (PBE).<sup>[33-34]</sup> For all of the structural optimizations, we set the kinetic energy cutoff to 520 eV and sampled the Brillouin zone with a  $k$ -spacing of  $0.3 \text{ \AA}^{-1}$ . The electronic convergence threshold is set to  $10^{-6} \text{ eV}$ , and the forces are converged to  $0.05 \text{ eV \AA}^{-1}$ . For  $\text{Cu}^{2+}$ -inserted MXene, we found 10  $\text{H}_2\text{O}$  molecules yield the best agreements with experimental data, with a  $c$  value of  $14.8 \text{ \AA}$ . Therefore, we adjusted the number of  $\text{H}_2\text{O}$  molecules so that we have a lattice parameter close to  $14.8 \text{ \AA}$ . For  $\text{Ni}^{2+}$ ,  $\text{Co}^{2+}$ , and  $\text{Mg}^{2+}$ , the resulting structures all have 11  $\text{H}_2\text{O}$  molecules, with the  $c$  lattice parameters being  $14.87 \text{ \AA}$ ,  $14.78 \text{ \AA}$ , and  $14.84 \text{ \AA}$  respectively.

#### **Ab initio molecular dynamics**

The AIMD calculations were performed with an NVT ensemble, where we fixed the number of atoms, volume, and temperature with a time step of 1 fs. The gamma point was used to sample the Brillouin zone with a reduced cutoff energy of 450 eV to lower the computational cost. The calculations involve three steps: (1) equilibration for 2 ps; (2) first production run for 40 ps; (3) second production run for 30 ps. Inspecting the final structure from the second step, we found the existence of isolated protons and  $\text{H}_2$  gas molecules. We speculated that they originate from an excess of H atoms in our setup which should not exist. Therefore, in the last step, we manually removed them before the last production run. The final structures from AIMD were used to calculate the density of states (DOS) and Bader charges.<sup>[35]</sup>

## ACKNOWLEDGMENTS

M.R.L., S.W. acknowledge support from the ETH Zurich start-up funding. The authors acknowledge DESY (Hamburg, Germany), a member of the Helmholtz Association HGF, for the provision of P64 Advanced X-ray Absorption Spectroscopy synchrotron radiation. Beamtime was allocated for proposal I-20221170 EC. The electrochemistry during beamtime was performed by using Biologic VMP-300 potentiostat of DESY/PETRA 3 beamline PO2.1. Furthermore, the authors acknowledge Diamond Light Source for the provision of B18 X-ray Absorption Spectroscopy synchrotron radiation where the beamtime was allocated for SP-30497. This work was granted access to the HPC resources of CINES under Allocation A0140910463 made by GENCI.

## REFERENCES

- [1] B. Anasori, M. R. Lukatskaya, Y. Gogotsi, *Nature Reviews Materials* **2017**, *2*, 16098.
- [2] M. R. Lukatskaya, S.-M. Bak, X. Yu, X.-Q. Yang, M. W. Barsoum, Y. Gogotsi, *Advanced Energy Materials* **2015**, *5*, 1500589.
- [3] M. R. Lukatskaya, S. Kota, Z. Lin, M.-Q. Zhao, N. Shpigel, M. D. Levi, J. Halim, P.-L. Taberna, M. W. Barsoum, P. Simon, Y. Gogotsi, *Nature Energy* **2017**, *2*, 17105.
- [4] M. R. Lukatskaya, O. Mashtalir, C. E. Ren, Y. Dall'Agnese, P. Rozier, P. L. Taberna, M. Naguib, P. Simon, M. W. Barsoum, Y. Gogotsi, *Science* **2013**, *341*, 1502-1505.
- [5] Z. W. Seh, K. D. Fredrickson, B. Anasori, J. Kibsgaard, A. L. Strickler, M. R. Lukatskaya, Y. Gogotsi, T. F. Jaramillo, A. Vojvodic, *ACS Energy Letters* **2016**, *1*, 589-594.
- [6] F. Shahzad, M. Alhabeab, C. B. Hatter, B. Anasori, S. Man Hong, C. M. Koo, Y. Gogotsi, *Science* **2016**, *353*, 1137-1140.
- [7] M. Zimmermann, L. R. H. Gerken, S. Wee, V. M. Kissling, A. L. Neuer, E. Tsolaki, A. Gogos, M. R. Lukatskaya, I. K. Herrmann, *Biomaterials Science* **2023**, *11*, 7826-7837.
- [8] A. VahidMohammadi, J. Rosen, Y. Gogotsi, *Science* **2021**, *372*, eabf1581.
- [9] M. D. Levi, M. R. Lukatskaya, S. Sigalov, M. Beidaghi, N. Shpigel, L. Daikhin, D. Aurbach, M. W. Barsoum, Y. Gogotsi, *Advanced Energy Materials* **2015**, *5*, 1400815.
- [10] M. Ghidui, S. Kota, J. Halim, A. W. Sherwood, N. Nedfors, J. Rosen, V. N. Mochalin, M. W. Barsoum, *Chemistry of Materials* **2017**, *29*, 1099-1106.
- [11] O. Mashtalir, M. Naguib, V. N. Mochalin, Y. Dall'Agnese, M. Heon, M. W. Barsoum, Y. Gogotsi, *Nature Communications* **2013**, *4*, 1716.
- [12] B. Wang, Q. Shu, H. Chen, X. Xing, Q. Wu, L. Zhang, *Metals* **2022**, *12*, 2022.
- [13] Y. Bai, C. Liu, T. Chen, W. Li, S. Zheng, Y. Pi, Y. Luo, H. Pang, *Angewandte Chemie International Edition* **2021**, *60*, 25318-25322.
- [14] D. Zhang, S. Wang, R. Hu, J. Gu, Y. Cui, B. Li, W. Chen, C. Liu, J. Shang, S. Yang, *Advanced Functional Materials* **2020**, *30*, 2002471.
- [15] H. Sun, C. Li, L. Yang, Y. Han, X. Yu, C.-P. Li, Z. Zhang, Z. Yan, F. Cheng, M. Du, *Proceedings of the National Academy of Sciences* **2023**, *120*, e2308035120.
- [16] Q. Zhao, C. Zhang, R. Hu, Z. Du, J. Gu, Y. Cui, X. Chen, W. Xu, Z. Cheng, S. Li, B. Li, Y. Liu, W. Chen, C. Liu, J. Shang, L. Song, S. Yang, *ACS Nano* **2021**, *15*, 4927-4936.
- [17] S. Wee, X. Lian, E. Vorobyeva, A. Tayal, V. Roddatis, F. La Mattina, D. Gomez Vazquez, N. Shpigel, M. Salanne, M. R. Lukatskaya, *ACS Nano* **2024**.
- [18] S. Bi, L. Knijff, X. Lian, A. van Hees, C. Zhang, M. Salanne, *ACS Nano* **2024**, *18*, 19931-19949.
- [19] Q. Gao, W. Sun, P. Ilani-Kashkouli, A. Tselev, P. R. C. Kent, N. Kabengi, M. Naguib, M. Alhabeab, W.-Y. Tsai, A. P. Baddorf, J. Huang, S. Jesse, Y. Gogotsi, N. Balke, *Energy & Environmental Science* **2020**, *13*, 2549-2558.
- [20] D. Z. Caralampio, B. Reeves, M. R. Beccia, J. M. Martínez, R. R. Pappalardo, C. den Auwer, E. Sánchez Marcos, *Molecular Physics* **2019**, *117*, 3320-3328.
- [21] J. Mareš, H. Liimatainen, K. Laasonen, J. Vaara, *Journal of Chemical Theory and Computation* **2011**, *7*, 2937-2946.

- [22] L. Verger, V. Natu, M. Ghidiu, M. W. Barsoum, *The Journal of Physical Chemistry C* **2019**, *123*, 20044-20050.
- [23] M. Ghidiu, J. Halim, S. Kota, D. Bish, Y. Gogotsi, M. W. Barsoum, *Chemistry of Materials* **2016**, *28*, 3507-3514.
- [24] M. R. Lukatskaya, D. Feng, S.-M. Bak, J. W. F. To, X.-Q. Yang, Y. Cui, J. I. Feldblyum, Z. Bao, *ACS Nano* **2020**, *14*, 15919-15925.
- [25] S. Calvin, *XAFS for Everyone*, 1st ed., CRC Press, Boca Raton, **2013**.
- [26] C. Christov, *Biomolecular Spectroscopy: Advances from Integrating Experiments and Theory*, Elsevier Science, **2013**.
- [27] T. A. Roelofs, W. Liang, M. J. Latimer, R. M. Cinco, A. Rompel, J. C. Andrews, K. Sauer, V. K. Yachandra, M. P. Klein, *Proc Natl Acad Sci U S A* **1996**, *93*, 3335-3340.
- [28] J. Yano, V. K. Yachandra, *Photosynthesis Research* **2009**, *102*, 241-254.
- [29] L. Martínez, R. Andrade, E. G. Birgin, J. M. Martínez, *Journal of Computational Chemistry* **2009**, *30*, 2157-2164.
- [30] A. P. Thompson, H. M. Aktulga, R. Berger, D. S. Bolintineanu, W. M. Brown, P. S. Crozier, P. J. in 't Veld, A. Kohlmeyer, S. G. Moore, T. D. Nguyen, R. Shan, M. J. Stevens, J. Tranchida, C. Trott, S. J. Plimpton, *Computer Physics Communications* **2022**, *271*, 108171.
- [31] G. Kresse, D. Joubert, *Physical Review B* **1999**, *59*, 1758-1775.
- [32] G. Kresse, J. Furthmüller, *Physical Review B* **1996**, *54*, 11169-11186.
- [33] J. P. Perdew, K. Burke, M. Ernzerhof, *Physical Review Letters* **1996**, *77*, 3865-3868.
- [34] J. P. Perdew, A. Ruzsinszky, G. I. Csonka, O. A. Vydrov, G. E. Scuseria, L. A. Constantin, X. Zhou, K. Burke, *Physical Review Letters* **2008**, *100*, 136406.
- [35] G. Henkelman, A. Arnaldsson, H. Jónsson, *Computational Materials Science* **2006**, *36*, 354-360.